

Faraday-Ramsey rotation measurement in a thin cell as an analogy to an atomic beam

MARK DIKOPOLTSEV,^{1,2,†,*} ELIRAN TALKER,^{1,†} YEFIM BARASH¹, NOA MAZURSKI¹ AND URIEL LEVY¹

¹*Institute of Applied Physics, The Faculty of Science, The Center for Nanoscience and Nanotechnology, The Hebrew University of Jerusalem, Jerusalem 91904, Israel*

²*Rafael Ltd., IL-31021, Haifa, Israel*

[†]*These authors contributed equally.*

^{*}*mark.dikopoltsev@mail.huji.ac.il*

Abstract: Atomic beams offer measurement capabilities for hot vapors but often require complex, bulky systems, limiting miniaturization. This study explores hot vapors in thin cells ($L = 30,5 \mu m$) as a simplified analogy to atomic beams. Coherence is maintained only for atoms moving parallel to the cell walls, as wall collisions randomize spin. By filtering non-parallel atoms, we mimic atomic beam behavior and observe the Faraday-Ramsey effect. Rubidium atoms are optically pumped with linearly polarized resonance radiation, evolving in a perpendicular magnetic field and probed via Faraday rotation. We believe that thin cell technology is paving the way for the miniaturization of atomic beam-based sensors.

1. Introduction

Atomic beams, consisting of alkali atoms, have a wide range of applications in modern scientific research and technology such as quantum information [1], high-precision measurements for studying fundamental constants [2], parity violation [3], and atomic clocks [4–6]. Optically transparent, hot vapor, alkali cells play a crucial role in various applications and studies involving atom-photon interactions, including portable atomic clocks [7], miniaturized magnetometers [8,9], and quantum gyroscopes [10]. These cells can be fabricated using MEMS technology and are characterized by their simplicity, reliability, and versatility. The control of alkali atom vapor density within the cells is achieved by regulating the cells temperature [11]. The geometric configuration of the cells significantly impacts the lifetime of atomic spins. Factors such as the shape and size of the cell, its optical depth, and atoms spin destruction due to the collision with the cell walls, influence the longevity of spin lifetime. These limitations impose restrictions on the potential for miniaturization. Extensive theoretical and experimental research has been conducted over the past decades to explore the possibilities for miniaturizing hot alkali vapor applications [12]. However, in miniaturized cells, frequent atom-wall collisions hinder the attainment of high-sensitivity sensors.

The ability to fabricate ultrathin alkali vapor cells, on the order of microns [13], endows unique features, making them valuable tools in specific research fields and applications. These cells enable the exploration of high alkali atom densities for studying all-optical switching and isolation [14] as well as nonlinear frequency conversion [15]. The thin cell geometry allows for 2D millimetric-scale magnetic gradiometry, which is usually achieved with separate cells [16]. Additionally, these cells provide a controlled environment for studying the properties and interactions of Rydberg atoms [17]. By incorporating spatial velocity filters, getters, and separate cell areas, atomic beams can also be generated [18].

The high rate of spin destruction due to wall collisions facilitates in-depth investigations into decoherence rates associated with various types of walls and anti-relaxation coatings. To mitigate the effects of wall collisions destruction, spin coherence can be preserved by using buffer gas. This changes the atomic motion from ballistic to a more diffusive-like and

potentially increases the mean time for wall collisions. However, the presence of buffer gas atoms can potentially affect a long-term stability due to temperature-dependent shifts in hyperfine atomic levels [19,20]. Additionally, adding buffer gas broadens the optical transition linewidth and mixes optical interaction with different hyperfine levels, making this technique inconvenient for applications that rely on interactions with single hyperfine levels [21]. Another approach involves applying anti-relaxation coatings, typically made of paraffin-like materials, to the cell walls to reduce the rate of spin destruction due to wall collisions [22,23]. This method is constrained by fabrication limitations, specifically the low temperatures that typical coatings can withstand during the fabrication process. Further reduction in cell dimensions leads to a dominant wall collision rate, impeding accurate measurements. Contrary to efforts aimed at minimizing the destructive effects of wall collision, this study leverages them as spatial filters for atomic coherence through velocity direction selection. This technique enables observation of the Faraday-Ramsey effect, which is usually measured using atomic beams or centimeter-sized alkali cells.

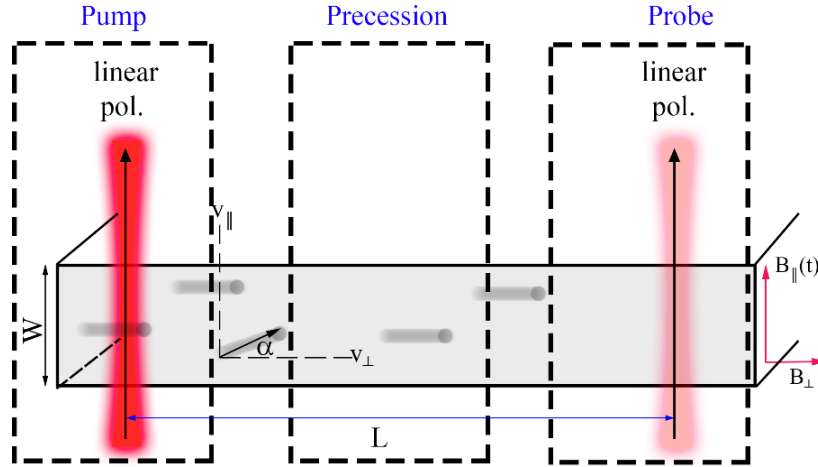


Fig. 1 Cartoon illustration showing the working principle of Faraday-Ramsey spectroscopy in a thin cell. In the optically pumped volume, atoms achieve a specific distribution of Zeeman states. In the precession area, only atoms with velocities parallel to the cell's long dimension propagate directly towards the probing beam and experience circulation of their Zeeman level's populations under the influence of the total magnetic field $B = \sqrt{B_{\parallel}^2 + B_{\perp}^2}$. The parallel magnetic field is slowly varied to scan the NLMO effect. The symbol α represents velocity direction. We define v_{\parallel} as the velocity parallel to the propagation direction of the pumping beam and v_{\perp} as the velocity perpendicular to the propagation direction of the pumping beam. Atoms that reach the volume illuminated by a probing beam participate in a photon polarization rotation process, which depends on the Bloch rotation of the atom's Zeeman levels.

2. NLMO Theory

Nonlinear magneto-optical (NLMO) experiments utilize the remarkable sensitivity of atomic spin coherence measurements, making them an invaluable tool for various high-resolution applications [24]. The phenomena underlying the NLMO effect elucidated in [25], and can be comprehensively described in three essential steps. The first step, shown in the 'Pump area' of Fig. 1, involves the generation of spin coherence through optical pumping using linearly polarized resonance radiation. As Fig. 2 illustrates, this process creates atomic alignment ($\Delta m = \pm 2$) in the ground state of a rubidium atom. The alignment is achieved by employing optical pumping with linearly polarized light. The second step, labeled 'Precession' in Fig. 1,

sees the coherence evolves due to its interaction with an external magnetic field. This interaction causes the spin orientation to precess around the magnetic field at the Larmor frequency. The evolution of this spin alignment is pivotal to the NLMO effect. The third and final step, termed ‘Probing’, involves optical detection of the medium’s altered properties. In a spatially separate probe region, atomic alignment is probed using a second laser beam in a polarimetric arrangement based on the Faraday Effect. This technique, known as Faraday-Ramsey spectroscopy, allows for the detection of time-averaged alignment. An ensemble of aligned atoms behaves as a medium with polarization selective properties such as birefringence and dichroism, which facilitate the detection process.

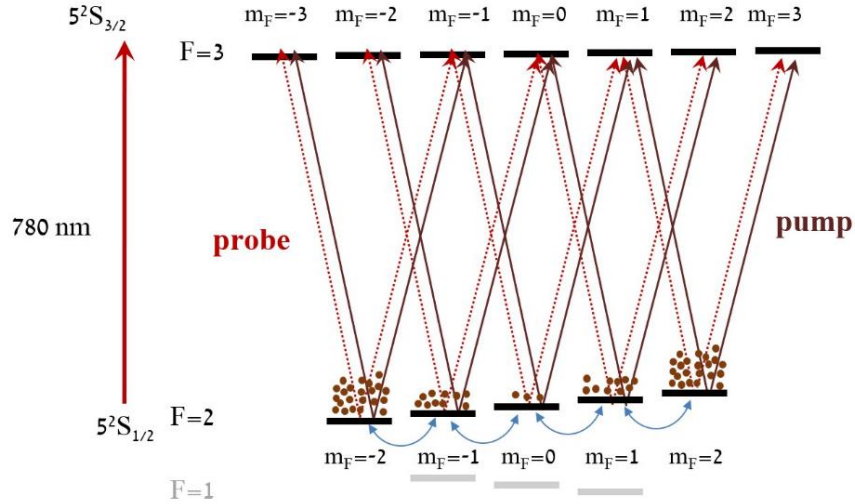


Fig. 2 Transition of ^{87}Rb on the D2 line from $F = 2$ to $F' = 3$, illustrated with Zeeman splitting. A detuned, linearly polarized pump beam, indicated by brown solid arrows in the \hat{z} direction creates a ground-state Zeeman levels population with a nonzero second moment $\langle m^2 \rangle > 0$. The magnetic field induces coherence mixing, represented by blue arrows. The probe beam, indicated by red dashed arrows is spatially separated from and parallel to the pump beam. It is linearly polarized and consists of σ^+ and σ^- circular polarizations. Each polarization propagates with a different index of refraction, dependent on the Zeeman coherence. This asymmetry induces birefringence during optical resonance interactions with the atoms.

In summary, NLMO experiments depend on the interplay among three key factors: the production of spin coherence through optical pumping, the subsequent evolution of this coherence in the presence of an external magnetic field, and the optical detection of the resulting changes in the medium's properties. The specific use of linearly polarized resonance radiation in the first step allows for the preparation of $\Delta m = \pm 2$ coherence. This evolves twice as fast in the interzone region as $\Delta m = \pm 1$ coherence does, leading to a halving of the resonance magnetic linewidth. If the birefringence axis is oriented at an angle θ - which is dependent on the B-field precession angle - with respect to the linear light polarization, we can simplify the Faraday rotation as follows in (1).

$$\Phi_F = \text{Im}(N_{\parallel} - N_{\perp}) \frac{\omega_L L}{2c} \sin(2\theta) \quad (1)$$

Here $\text{Im}(N_{\parallel} - N_{\perp})$ represent the imaginary parts of the index of refraction for the light polarized parallel and perpendicular to the axis of birefringence, respectively. The separation

length between the pump and the probe beam L , and ω_L represents the Larmor frequency. One can show that $\text{Im}(N_{\parallel} - N_{\perp})$ is proportional to (2) [26,27]:

$$\text{Im}(N_{\parallel} - N_{\perp}) \propto \langle 3F_z^2 - F^2 \rangle = \langle 2F_z^2 - (F_x^2 + F_y^2) \rangle \quad (2)$$

With the z-axis serving as the quantization axis, we can express the total macroscopic angular momentum of the atoms in the hyperfine ground state F as follows:

$$\langle \hat{F}_x \rangle = \left\langle \frac{1}{2} (\hat{F}_+ + \hat{F}_-) \right\rangle = N \sum_{m=-F}^{F-1} \frac{A(F, m)}{2} (\rho_{m+1, m} + \rho_{m, m+1}) \quad (3)$$

$$\langle \hat{F}_y \rangle = \left\langle \frac{1}{2i} (\hat{F}_+ - \hat{F}_-) \right\rangle = N \sum_{m=-F}^{F-1} \frac{A(F, m)}{2i} (\rho_{m+1, m} - \rho_{m, m+1}) \quad (4)$$

$$\langle \hat{F}_z \rangle = N \sum_{m=-F}^F m \rho_{m, m} \quad (5)$$

Where $\hat{F}_{+,-}$ are the rising and lowering operators for the spin along \hat{z} respectively and $\rho_{i,j}$ is the density operator that describe the state of the atoms and $i, j = -F, \dots, F$ parametrize the Zeeman magnetic sublevels. For more details on the density operators see [28] Part 1.

To calculate the line shape, we must consider Doppler broadening. The damping of the Ramsey fringes is a consequence of the finite width of the Maxwellian distribution $\mathcal{M}(v_{\parallel})$ of the longitudinal velocities relative to the pump beam and the average of the Larmor-rotating part of the atomic polarization, $\sin(2\omega_L t_{\perp})$. Hence, we can express the Faraday rotation as shown in (6). The first term is the linear component, which accounts for the line shape from the broader structure, with c_1 and c_2 as fitting parameters. The second term involves the velocity distribution, derived from the cell parameters. The Maxwellian distribution is given by (7).

The argument $\eta = L|v_{\parallel}|/Wu = \tilde{t}_{\perp}/t_{\parallel}$ represents relations between the longitudinal and mean transverse propagation times of the particles in the cell where $\tilde{t}_{\perp} = L/u$ and $t_{\parallel} = W/|v_{\parallel}|$ [28] Part 2. The gyromagnetic ratio of the atoms is given by $\omega_L = \gamma B$, with $\gamma = g_F \mu_B / \hbar$ and B as the total magnetic field. The relaxation of the spin alignment due to atomic collisions described by $e^{-\Gamma t_{\perp}}$, where Γ is the decoherence rate and $t_{\perp} = L/v_{\perp}$ atoms perpendicular propagation time, with L being the distance between the pump and probe beams.

$$\Phi_F(v_{\parallel}) \propto c_1 \omega_L + c_2 \int_{-\infty}^{\infty} \mathcal{M}(v_{\parallel}) \cdot \sin(2\omega_L t_{\perp}) \cdot e^{-\Gamma t_{\perp}} dv_{\parallel} \quad (6)$$

$$\mathcal{M}(v_{\parallel}) \propto \frac{1}{\pi} e^{-(\eta)^2} - \frac{1}{\sqrt{\pi}} \eta (1 - \text{erf}(\eta)) \quad (7)$$

In this study, we exploit the fact that, in a thin cell, the atoms contributing to the signal move parallel to the cell walls. By applying the Faraday-Ramsey scheme, we achieve directional filtering of the propagating coherences, measuring only those atoms moving parallel to the cell walls. This specific geometry allows us to attain coherence lifetimes typical of millimeter-sized cells, in the range of single microseconds, within an ultra-thin micron-sized cell, where the expected coherence lifetime is on the order of ten nanoseconds.

3. Experiment

Fig. 3 shows the scheme of the experimental setup. The experiments were performed on the D2 resonance line ($\lambda = 780 \text{ nm}$). The resonance transition was set to $F_g = 2 \rightarrow F_e = 3$ and stabilized using the Doppler-free dichroic atomic laser lock [29]. The laser beam was split into two beams using a non-polarizing beam splitter with a ratio of 90:10. The intensities of the two beams were adjusted using variable neutral-density filters. The power of the linearly polarized pump beam was set to 12 mW . The diameter of the pump beam was increased using beam expander and then sent through an axicon lens to generate a ring-shaped beam. The diameter of the ring was varied by adjusting the position of the axicon lens. The linearly polarized probe beam, 1 mm in diameter and $150 \text{ }\mu\text{W}$ in power, passed through the center of the pumping ring.

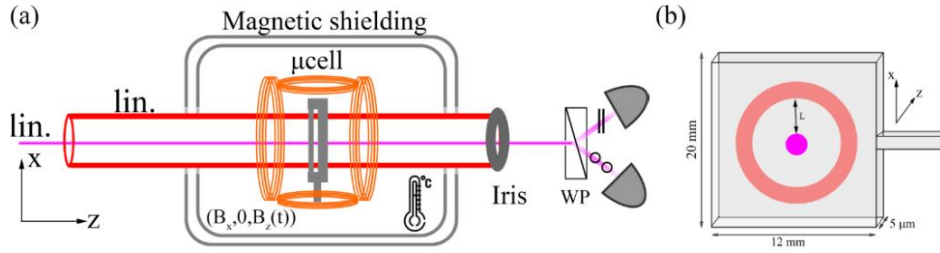


Fig. 3. (a) Cartoon of the experimental setup used for the Faraday rotation measurement. A linear pump beam (red) and probe beam (magenta) impinge on the cell, which is heated to 120°C and situated in a well-defined magnetic environment created by external coils and μ -metal magnetic shielding. The pump beam is spatially filtered by an iris upon exiting the cell, while the probe beam is directed to a Wollaston Prism (WP) that spatially separates its polarization components. (b) Schematic sketch of the probe and pump illumination configuration within the cell's interior volume, from a top view.

We used the ring-shaped pump beam to leverage the spatial benefits of the thin cell along with the geometry of the physical configuration. Due to the radial symmetry, both the velocity distribution's dependence on cell geometry and the Zeeman levels' population and coherence dependence on the magnetic field remained constant. This technique significantly improved pumping efficiency and, consequently, increased the flux of coherent atoms to the probe.

By changing the pump beam ring diameter in a range from 1 mm up to 8 mm , we could control the distance between the probe and pump beam. Faraday rotation measurement of the probe beam was conducted using a Wollaston prism, which spatially separated the probe beam to its polarization components and collected them using two channels of a balanced photodetector. The plane direction was tuned to equalize the intensity of both components while the probe wavelength was tuned to be off resonance. A Faraday rotation signal was observed when probe's resonant interaction with the atoms induced a Faraday rotation effect. As shown in Fig. 3, the dimensions of the homemade ^{87}Rb vapor cell are 20 mm height and 12 mm width. Two cell thicknesses were used: 5 and $30 \text{ }\mu\text{m}$. Cell fabrication was done using lithography, reactive ion etching and anodic bonding. The cell was heated up to 120°C , leading to a rubidium atomic density of $n_{\text{Rb}} \approx 2 \times 10^{13} \text{ cm}^{-3}$. The estimated polarized atom flux at the largest pump-to-probe separation is $F_{\text{Rb}} \approx 2.2 \times 10^9 \text{ sec}^{-1}$ [28] Part 3.

To ensure a well-controlled magnetic environment, the cell is placed inside four layers of mu-metal magnetic shielding to cancel out stray magnetic field in the lab. Inside this shielding, we place two sets of Helmholtz coils. The first set generates a static magnetic field perpendicular to the direction of beam propagation to mix the Zeeman levels coherence and to break the degeneracy in the ground-state sublevels, as presented in Fig. 2. The second set of coils generates a scanning magnetic field along the direction of the beam to alter the Larmor rotation rate of atomic polarization coherence, thereby scanning the Ramsey fringes. By

measuring the Faraday rotation as a function of magnetic field intensity, one can observe the Faraday-Ramsey spectroscopy.

4. Experimental results

We sorted the velocities of atoms by direction using the effect of wall collisions and applied specific magnetic fields. As described in (6) the atoms exhibited Larmor dynamics. At operating temperature of 120°C , collisions leading to interatomic spin decoherence, which cause an exponential decay at the rate Γ , were not significant for most of our measurements. However, during standard Larmor rotation, represented in the model by $\sin(2\omega_L t_{\perp})$, atoms with different planar velocities reached the probing area at different times and because of velocities integration, relative dephasing occurred between them, and it is the dominant decoherence process in the measured conditions.

In Fig. 4 and Fig. 5 we present the theoretical and experimental line shapes of the Faraday-Ramsey rotation for cell thickness of 30 and 5 microns respectively as a function of the external magnetic field B , which is the second term in equation (6). The first term represents a linear Faraday rotation and is omitted from the experimental measurement using the calibration measurement without the optical pumping beam, as described in [28] Part 5. The direction of the scanned magnetic field is parallel to the propagation direction of the laser beams. In the experiment, the magnetic field varies slowly (10Hz), ensuring that the period of a magnetic sweep is much longer than the typical atom transit time across the cell. The spatially displaced pump and probe beams have the same wavelength.

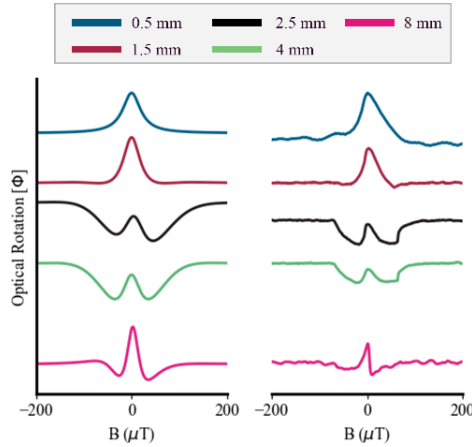


Fig. 4. Theoretical (left) and experimental (right) results of Faraday-Ramsey rotation for the $F_g = 2 \rightarrow F_e = 3$ transition in ^{87}Rb with a $30\mu\text{m}$ cell thickness. The results are shown for linearly polarized pump and probe beams at different inner diameters of the pump beam, as indicated by the top legend.

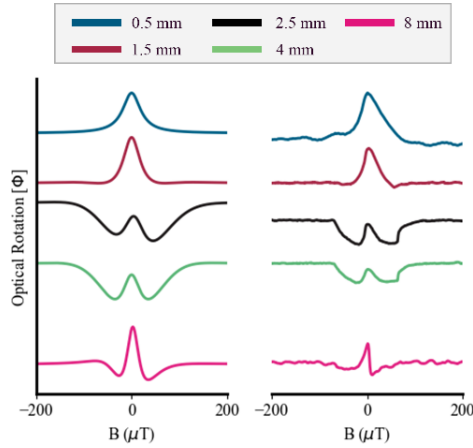


Fig. 5. Theoretical (left) and experimental (right) results of the Faraday-Ramsey rotation for the $F_g = 2 \rightarrow F_e = 3$ transition in Rb^{87} with a $5\mu\text{m}$ cell thickness. The results are shown for linearly polarized pump and probe beams at different inner diameters of the pump beam as indicated by the top legend.

The results clearly show that increasing the distance between the probe and the pump beams decreases the magnetic linewidth due to longer spin state precession time that causes better filtering. When comparing the magnetic linewidth between $5\mu\text{m}$ and $30\mu\text{m}$ cells, we observe that the linewidth for the $5\mu\text{m}$ cell is narrower than that for the $30\mu\text{m}$ cell, owing to more effective velocity filtering. Essentially, reducing the cell thickness allows for better collimation of the “coherent beam” of atoms.

In Fig. 6, we demonstrate the good agreement between the theoretical model and the experimental results for a pump beam diameter of 8mm and a cell thickness of $5\mu\text{m}$. In the theoretical model, we set the Rabi frequency of the pump beam Ω_{pu} to 50MHz and that of the probe beam Ω_{pr} to 2MHz [28] Part 1. Additionally, the constant magnetic field perpendicular to the direction of the pump beam (B_{\perp}) was set to $20\mu\text{T}$, as it was conducted in experiment.

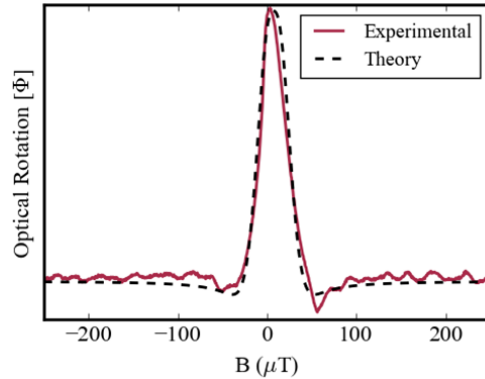


Fig. 6. A comparison of experimental results with the theoretical model, focusing on a cell thickness of $5\mu\text{m}$ and an 8mm diameter of the pump beam.

Next, we derived the magnetic linewidth (FWHM – Full Width Half Maximum) for all measured beam separation distances for both cell thicknesses. In Fig. 7 we present results that are consistent with both the model and the geometrical intuition underlying atomic beam design principles. We experimentally verified that the limiting factor of the FWHM is the atomic spin

precession decay, Γ (6) which is dominantly caused by the self, alkali spin exchange collisions process. This process depends on the vapor's density. Therefore, for a given alkali density, there is an optimal separation length on the order of a spin exchange mean free path λ_{SE} [28] Part 3. Beyond this optimal length, increasing the separation distance does not further improve the resonance linewidth.

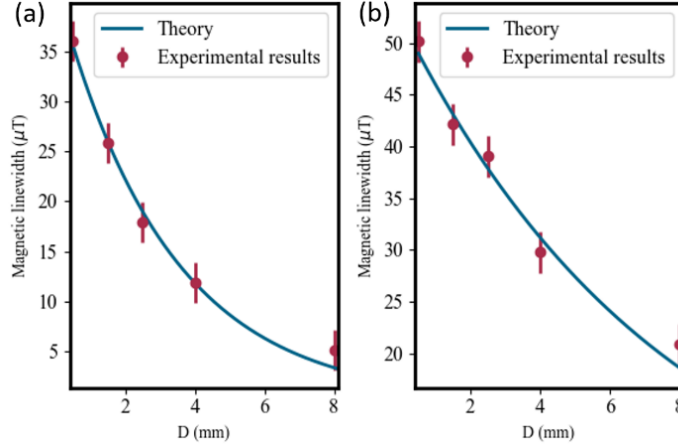


Fig. 7. Theoretical and measured magnetic linewidth as a function of the inner diameters of the pump beam for (a) $5\mu\text{m}$ and (b) $30\mu\text{m}$ cell thickness.

5. Conclusions

In this work we provide an analogy to the measurement of Faraday-Ramsey rotation using thin, alkali hot vapor cells fabricated through a chip-scale manufacturing process. These cells contain rubidium atoms polarized by a resonant optical beam. The thin cell geometry enables spatial velocity filtering of the polarized atoms due to wall-induced spin-destruction collisions. Atoms propagating parallel to the cell walls behave as an "atomic like" beam with an estimated flux of $F_{\text{Rb}} \cong 2 \times 10^9 \text{ sec}^{-1}$. We observed the Faraday-Ramsey effect using a radial pumping geometry that allows to maintain symmetry and to increase the signal-to-noise ratio. The measured results agree with the predicted model. Briefly, the ensemble of atoms has a central velocity, and there is a Gaussian statistical distribution of velocities due to Doppler velocity broadening, which contributes to the magnetic resonance linewidth. The narrower the cell, the more confined the velocity distribution, making the effect of spatial filtering of velocities more prominent. Measurements of different magnetic resonance line shapes at various distances between the pump and probe beams, and for both cell widths, fit the proposed model.

The coherent atomic flux in our presented configuration of the thin cell is limited by low alkali density, which results in a relatively weak signal. Alkali-spin exchange collisions also constrain the maximum density, which, in turn, affects the magnetic linewidth that can be achieved. To further enhance the density, we propose increasing the temperatures and using cesium atoms instead of rubidium. To bypass the restrictions imposed by spin exchange process, we suggest employing a spatial filter, along with the addition of a dispenser and a temperature gradient. These improvements can increase the atomic beam like flux production and reduce the density of unpolarized atoms, thereby decreasing spin-exchange rate decoherence.

The primary advantages of using a thin-cell technique to generate an atomic beam-like structure include its simplicity, potential for device miniaturization, and scalability. This

method facilitates a wide range of applications that traditionally utilize atomic beams, including frequency standards, gradiometry, and Rydberg atom research, among others.

Supplemental document. See Supplemental information [28] for supporting content.

References

1. G. Buser, R. Mottola, B. Cotting, *et al.*, "Single-Photon Storage in a Ground-State Vapor Cell Quantum Memory," *PRX Quantum* 3, 20349 (2022).
2. N. F. Ramsey, "A Molecular Beam Resonance Method with Separated Oscillating Fields," *Physical Review* 78, 695–699 (1950).
3. C. S. Wood, S. C. Bennett, D. Cho, *et al.*, "Measurement of Parity Nonconservation and an Anapole Moment in Cesium," *Science* (1979) 275, 1759–1763 (1997).
4. J. Vanier, A. Godone, F. Levi, *et al.*, "Atomic clocks based on coherent population trapping: basic theoretical models and frequency stability," in *IEEE International Frequency Control Symposium and PDA Exhibition Jointly with the 17th European Frequency and Time Forum, 2003. Proceedings of the 2003* (2003), pp. 2–15.
5. J. D. Elgin, T. P. Heavner, J. Kitching, *et al.*, "A cold-atom beam clock based on coherent population trapping," *Appl Phys Lett* 115, 033503 (2019).
6. M. A. Lombardi, T. P. Heavner, and S. R. Jefferts, "NIST Primary Frequency Standards and the Realization of the SI Second," *NCSLI Measure* 2, 74–89 (2007).
7. C. Carlé, M. A. Hafiz, S. Keshavarzi, *et al.*, "Pulsed-CPT Cs-Ne microcell atomic clock with frequency stability below 2×10^{-12} at 105 s," *Opt. Express* 31, 8160–8169 (2023).
8. A. Fabricant, I. Novikova, and G. Bison, "How to build a magnetometer with thermal atomic vapor: a tutorial," *New J Phys* 25, 025001 (2023).
9. O. Alem, R. Mhaskar, R. Jiménez-Martínez, *et al.*, "Magnetic field imaging with microfabricated optically-pumped magnetometers," *Opt Express* 25, 7849 (2017).
10. R. M. Noor and A. M. Shkel, "MEMS Components for NMR Atomic Sensors," *Journal of Microelectromechanical Systems* 27, 1148–1159 (2018).
11. Y. Gao, D. Ma, S. Jiang, *et al.*, "A novel oven structure for improving temperature uniformity of vapor cell in atomic sensors," *Results Phys* 47, 106339 (2023).
12. J. Kitching, "Chip-scale atomic devices," *Appl Phys Rev* 5, 031302 (2018).
13. E. Talker, R. Zektzer, Y. Barash, *et al.*, "Atomic spectroscopy and laser frequency stabilization with scalable micrometer and sub-micrometer vapor cells," *Journal of Vacuum Science & Technology B, Nanotechnology and Microelectronics: Materials, Processing, Measurement, and Phenomena* 38, (2020).
14. E. Talker, P. Arora, M. Dikopoltsev, *et al.*, "Optical isolator based on highly efficient optical pumping of Rb atoms in a miniaturized vapor cell," *Journal of Physics B: Atomic, Molecular and Optical Physics* 53, 045201 (2020).
15. Y. Sebbag, Y. Barash, and U. Levy, "Generation of coherent mid-IR light by parametric four-wave mixing in alkali vapor," in *2018 Conference on Lasers and Electro-Optics (CLEO)* (2018), pp. 1–2.
16. D. Sheng, A. R. Perry, S. P. Krzyzewski, *et al.*, "A microfabricated optically-pumped magnetic gradiometer," *Appl Phys Lett* 110, (2017).
17. J. A. Gordon, C. L. Holloway, A. Schwarzkopf, *et al.*, "Millimeter wave detection via Autler-Townes splitting in rubidium Rydberg atoms," *Appl Phys Lett* 105, (2014).
18. G. D. Martinez, C. Li, A. Staron, J. Kitching, *et al.*, "A chip-scale atomic beam clock," *Nat Commun* 14, 3501 (2023).
19. R. Boudot, D. Miletic, P. Dziuban, *et al.*, "First-order cancellation of the Cs clock frequency temperature-dependence in Ne-Ar buffer gas mixture," *Opt Express* 19, 3106 (2011).
20. L. Wu, J. Shang, Y. Ji, *et al.*, "Influence of Buffer-Gas Pressure Inside Micro Alkali Vapor Cells on the Performance of Chip-Scale SERF Magnetometers," *IEEE Trans Compon Packaging Manuf Technol* 8, 621–625 (2018).
21. A. Berrebi, M. Dikopoltsev, O. Katz, *et al.*, "Optical protection of alkali-metal atoms from spin relaxation," *ArXiv* (2022).
22. S. J. Seltzer, D. J. Michalak, M. H. Donaldson, *et al.*, "Investigation of antirelaxation coatings for alkali-metal vapor cells using surface science techniques," *J Chem Phys* 133, (2010).
23. R. Straessle, M. Pellaton, C. Affolderbach, *et al.*, "Microfabricated alkali vapor cell with anti-relaxation wall coating," *Appl Phys Lett* 105, (2014).
24. D. Budker, W. Gawlik, D. F. Kimball, *et al.*, "Resonant nonlinear magneto-optical effects in atoms," *Rev Mod Phys* 74, 1153–1201 (2002).
25. B. Schuh, S. I. Kanorsky, A. Weis, *et al.*, "Observation of Ramsey fringes in nonlinear Faraday rotation," *Opt Commun* 100, 451–455 (1993).

26. A. Weis, S. I. Kanorsky, and J. Wurster, "Quantitative interpretation of the nonlinear Faraday effect as a Hanle effect of a light-induced birefringence," *Journal of the Optical Society of America B* 10, 716 (1993).
27. S. I. Kanorsky, A. Weis, J. Wurster, *et al.*, "Quantitative investigation of the resonant nonlinear Faraday effect under conditions of optical hyperfine pumping," *Phys Rev A (Coll Park)* 47, 1220–1226 (1993).
28. Dikopoltsev Mark, Talker Eliran, Barash Yefim, *et al.*, "Supplementary information - Faraday-Ramsey rotation measurement in a thin cell as analogy to atomic beam," (2024).
29. K. L. Corwin, Z.-T. Lu, C. F. Hand, *et al.*, "Frequency-stabilized diode laser with the Zeeman shift in an atomic vapor," *Appl Opt* 37, 3295 (1998).

FARADAY-RAMSEY ROTATION MEASUREMENT IN A THIN CELL AS AN ANALOGY TO AN ATOMIC BEAM: SUPPLEMENTAL DOCUMENT

1. Optical Bloch Equation (OBE)

We consider atoms illuminated by a laser light, resonant with the $F_g = 2 \rightarrow F_e = 3$ transition as for the D_2 line of the Rb^{87} atoms. A static magnetic field B_z is applied collinear to the laser light propagation to set the quantization axis to be at the same direction of the light beam and will be denoted as B_{\parallel} . A magnetic field B_x simultaneously applied along the perpendicular axis will be denoted as B_{\perp} . A linearly polarized probing laser beam propagating along the parallel axis.

The master equation for the density matrix operators is given by (S1) where \mathcal{L} is the Liouville operators that describe the decay process of the system. The unperturbed element of the Hamiltonian (S2) is the energy of the sublevels of the state. The Hamiltonian of spins subjects to a magnetic field \mathbf{B} is given by (S3). In our work a slowly varying magnetic field with strength $B_z(t)\hat{z}$ applied together with a constant magnetic field $B_x\hat{x}$ in the perpendicular direction to mix Zeeman levels coherence. Hence, the above Hamiltonian for a single atom is given by (S4). The interaction of atoms with light \mathcal{V} in the dipole approximation is described by (S5) where (S6) and (S7) are the pump and probe beam Rabi frequencies correspondingly. We use the same laser beam, split unequally in power, so that $\Omega_{pr} < \Omega_{pu}$ and $\omega_{pu} = \omega_{pr}$.

$$\partial_t \rho = -\frac{i}{\hbar} [\mathcal{H}_B + \mathcal{H}_0 + \mathcal{V}(t), \rho] + \mathcal{L}\{\rho\} \quad (\text{S1})$$

$$\mathcal{H}_0 = E_0(F) \quad (\text{S2})$$

$$\mathcal{H}_B = g_F \mu_B \vec{F} \cdot \vec{B} \quad (\text{S3})$$

$$\mathcal{H}_B = g_F \mu_B (B_z F_z + B_x F_x) \quad (\text{S4})$$

$$\mathcal{V}(t) = \frac{\hbar}{2\sqrt{2}} \left[\sum_{g_k} \Omega_{pu}(t) (\rho_{g_k, g_{k+1}} + \rho_{g_k, g_{k-1}}) + \Omega_{pr}(t) (\rho_{g_k, g_{k+1}} + \rho_{g_k, g_{k-1}}) \right] + C. C. \quad (\text{S5})$$

$$\Omega_{pu}(t) = \Omega_{pu} \cdot \text{rect} \left(\frac{t - T_1}{\frac{T_1}{2}} \right) \exp(-i\omega_{pu}t) + c. c. \quad (\text{S6})$$

$$\Omega_{pr}(t) = \Omega_{pr} \cdot \text{rect} \left(\frac{t - (T_2 + \frac{3}{2}T_1)}{\frac{T_1}{2}} \right) \exp(-i\omega_{pr}t) + c. c. \quad (\text{S7})$$

Here T_1 is the time of flight of the atoms inside the beam with a diameter of 0.5 mm (the beam diameter of the pump and the probe beam are the same), T_2 is the dark time where both the pump and the probe beam intensity are zero. We can write the OBE for a closed system using following notation: $|e_i\rangle = |F_e, m_i\rangle$, $|g_i\rangle = |F_g, m_i\rangle$, as (S8).

$$\dot{\rho}_{e_i e_j} \Big|_{B_x} = -i \frac{\mu_B B_x}{2\hbar} g_e \{c\} \quad (\text{S8})$$

$$\dot{\rho}_{e_i e_j} = -\left(i\omega_{e_i e_j} + \Gamma\right)\rho_{e_i e_j} + \frac{i}{\hbar} \sum_{g_k} \left(\rho_{e_i g_k} V_{g_k e_j} - V_{e_i g_k} \rho_{g_k e_j}\right) \quad (\text{S9})$$

$$\dot{\rho}_{e_i g_j} = -\left[i\omega_{e_i g_j} + \frac{\Gamma}{2}\right]\rho_{e_i g_j} + \frac{i}{\hbar} \left(\sum_{e_k} \rho_{e_i e_k} V_{e_k g_j} - \sum_{g_k} V_{e_i g_k} \rho_{g_k g_j}\right) \quad (\text{S10})$$

$$\begin{aligned} \dot{\rho}_{g_i g_j} = & -i\omega_{g_i g_j} \rho_{g_i g_j} + \frac{i}{\hbar} \sum_{e_k} \left(\rho_{g_i e_k} V_{e_k g_j} - V_{g_i e_k} \rho_{e_k g_j}\right) \\ & + \left(\frac{d}{dt} \rho_{g_i g_j}\right)_{SE} \end{aligned} \quad (\text{S11})$$

The spontaneous emission repopulation terms for the density matrix evolution given by (S12). By solving the above equation, we can calculate the macroscopic angular momentum of the atoms in the hyperfine ground state F.

$$\begin{aligned} & \left(\frac{d}{dt} \rho_{g_i g_j}\right)_{SE} \\ & = (2F_e + 1)\Gamma \sum_{\substack{(q, q' = -F_e, F_e), \\ (p = -1, 1)}} (-1)^{p-k-q'} \begin{pmatrix} F_g & 1 & F_e \\ -k & p & q \end{pmatrix} \rho_{e_q e_{q'}} \begin{pmatrix} F_e & 1 & F_g \\ -q' & -p & k' \end{pmatrix} \end{aligned} \quad (\text{S12})$$

2. Angular distribution

Consider a 2D diagram as shown Fig. S1 for a specific angle $\alpha = \text{atan}\left(\frac{W-z}{L}\right)$, where $z = W - L \cdot \tan(\alpha)$. Only particles moving through the section $ls = z$ of the pump beam can reach the probe beam. Assuming a homogeneous particles density in the entire cell, the number of particles in a small interval $d\alpha$ is given by (S13).

$$\begin{aligned} f(\alpha) d\alpha = & A(W - L \cdot \tan(\alpha)) d\alpha \\ & - \arctan\left(\frac{W}{L}\right) \leq \alpha \leq \arctan\left(\frac{W}{L}\right) \end{aligned} \quad (\text{S13})$$

Where A is a normalization constant, and we have extended α to include the negative angles as well. For a thin cell, $W \ll L$ and hence we can linearize this distribution function (S14). By using a total number of pumped particles N_{pu} , the angular distribution can be normalized (S15). A total volume V_{pu} illuminated in the $5\mu\text{m}$ ($30\mu\text{m}$) cell by the ring-shaped pumping beam with the ring width $w_{pu} = 0.5\text{mm}$ and ring inner diameter $D = 8\text{mm}$ when $L = D/2 = 4\text{mm}$ given by (S16).

$$f(\alpha) d\alpha \approx A(W - L \cdot \alpha) d\alpha \quad (\text{S14})$$

$$N_{pu} = 2 \int_0^{W/L} f(\alpha) d\alpha = A \frac{W^2}{L} \quad (\text{S15})$$

$$V_{pu} = 2\pi L w_{pu} W = 6.3 \times 10^{-5} \text{cm}^3 \quad (3.8 \times 10^{-4} \text{cm}^3) \quad (\text{S16})$$

Multiplying this volume by the density at the working point $n_{Rb}@120^\circ C \cong 2 \times 10^{13} cm^{-3}$ one obtains the number of particles:

$$N_{pu} = n_{Rb} * V_{pu} = 1.3 \cdot 10^9 \quad (7.7 \times 10^9) \quad (S17)$$

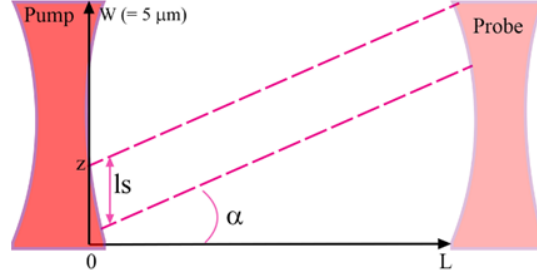


Fig. S1 Schematic 1D view of the pump and probe beam. For a specific angle $\approx (W - z)/l$, particles moving from the section ls of the pump can move through the probe beam.

3. Flux calculation of the coherent atoms

The number of pumped atoms given in (S17) $N_{pu} = n_{Rb} * V_{pu}$. We provide an approximated calculation of particles with a velocity direction towards the probe beam as presented in Fig. S2. We assume isotropic velocity directions within the pumped area and thus we choose to use a spherical geometry for atoms propagation model. For each pumped atom we create a spherical spatial propagation direction distribution with radius L . We calculate the approximated, effective area cross-section of this sphere $S_{sphere} = 4\pi L^2$ with a probe beam transversal projection $S_{probe-side} = 2R_{PR}W$ so their area's relation is approximately $R_{es} = R_{PR}W/2\pi L^2$ and this is atom's probability to reach the probing area before the wall. The total probed number of coherent atoms is: $N_{exp} = R_{es}N_{pu}$. To roughly estimate atoms flux, we will take a peak atom velocity $v_p = \sqrt{2k_bT/m_{rb}} = 277m/sec$ so the achieved flux is $F_{meas} = N_{exp}v_p/L$. For the $5\mu m$ ($30\mu m$) cell thickness, $0.5mm$ pump beam width and $0.5mm$ probe beam radius, the estimated flux is: $F_{meas} = 2.2 \cdot 10^9 sec^{-1}$ ($7.9 \cdot 10^{10} sec^{-1}$).

Usually, the dominant decoherence process in the hot vapor alkali cell with a high atoms density is the spin-exchange process due to angular momentum conserving collisions [1]. Mean free path to the spin exchange interaction is given by (S18), $\sigma_{SE} = 1.9 \times 10^{-14} cm^2$ is the cross-section for the spin exchange and the rate is given by (S19). Here $V_{Rb} = \sqrt{4k_B T/\pi m_{rb}}$ is the relative thermal velocity of the rubidium atoms with rubidium atom's mass - m_{rb} .

$$\lambda_{SE} = \frac{1}{\sqrt{2}n_{Rb}\sigma_{SE}} \quad (S18)$$

$$R_{SE} = \sqrt{2}V_{Rb}\lambda_{SE} \quad (S19)$$

We calculate a spin exchange mean free path and rate for the present working point: $\lambda_{SE}(120^\circ C) \approx 18mm$, $R_{SE}(120^\circ C) \approx 1.7 \times 10^4 sec^{-1}$.

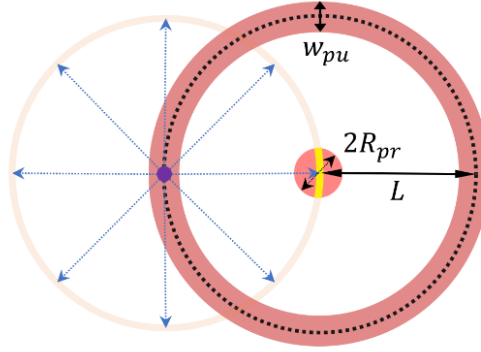


Fig. S2 . In the schematic 2D sketch, we assume isotropic velocity directions within the pumped area, where L represents the pump beam ring radius, w_{pu} corresponds to the pump beam ring width, and R_{pr} denotes the probe beam radius. The purple dot indicates the location of a single rubidium atom, and the blue dotted arrows represent its possible propagation directions

4. Transverse velocity distribution

Here we present a simplified 2D model for the transverse velocity distribution, which closely describes our experimental geometry due to its radial symmetry. The longitudinal and transverse velocities of the particles are correlated based on their direction of movement (see Fig. 1 in the main text):

$$\frac{v_{\parallel}}{v_{\perp}} = \tan(\alpha) \quad (\text{S20})$$

For atoms contributing to the signal, we have $v_{\parallel} \ll v_{\perp}$ because the cell width W is much smaller than the cell length L , as dictated by the cell geometry. In fact, there exists a maximum angle value α_{max} given in (S21).

$$\tan(\alpha_{max}) = \frac{W}{L} = \frac{v_{\parallel}^{max}}{v_{\perp}^{min}} \rightarrow v_{\perp, min} = \frac{L}{W} v_{\parallel}^{max} \quad (\text{S21})$$

Considering a small-angle approximation, we can represent a transversal velocity direction derivative using $dv_{\perp} \approx v d\alpha$. The distribution of particles with a transverse velocity v_{\perp} and longitudinal velocity v_{\parallel} is given by (S22), with $f(\alpha)$ being the approximated angular distribution function given in (S14), and $f_{MB}(v)$ being the Maxwell-Boltzmann velocity distribution (S23), with the most probable velocity of the atoms $u = \sqrt{k_B T/m}$, where k_B is the Boltzmann constant, T is the atomic temperature, and m is the atomic mass. Therefore, the transverse velocity distribution function is (S24). Integration by dv leads to the Maxwellian distribution of the longitudinal velocities (S25), Where $erf(x) = 2\pi^{-1/2} \int_0^x \exp(-y^2) dy$. Argument $\eta = L|v_{\parallel}|/Wu = \tilde{t}_{\perp}/t_{\parallel}$ represents relations between the longitudinal and mean transverse times of particles propagation in the cell: $\tilde{t}_{\perp} = L/u$, $t_{\parallel} = W/|v_{\parallel}|$.

$$f(v_{\parallel}, v_{\perp}) dv_{\parallel} dv_{\perp} = f(\alpha) f_{MB}(v) d\alpha dv dv_{\parallel} \quad (\text{S22})$$

$$f_{MB}(v) = \pi^{-\frac{1}{2}} \cdot \frac{v}{u^2} \exp\left(-\frac{v^2}{u^2}\right) \quad (\text{S23})$$

$$f_{\parallel} dv_{\parallel} = \int_{v_{\perp, min}}^{\infty} A \left(W - \frac{L \cdot v_{\parallel}}{v} \right) \pi^{-\frac{1}{2}} \cdot \frac{v}{u^2} \exp \left(-\frac{v^2}{u^2} \right) dv dv_{\parallel} \quad (\text{S24})$$

$$\mathcal{M}(v_{\parallel}) dv_{\parallel} = f_{\parallel} dv_{\parallel} \approx \frac{\sqrt{\pi} A W}{2} \left(\frac{1}{\pi} e^{-(\eta)^2} - \frac{1}{\sqrt{\pi}} \eta (1 - \text{erf}(\eta)) \right) dv_{\parallel} \quad (\text{S25})$$

In Fig. S3, we plot the transverse velocity distribution for different cell thicknesses. In both cases, the transverse velocity is lower than 10 m/sec indicating that most of the atoms contributing to the signal are moving in a grazing direction relative to the surface.

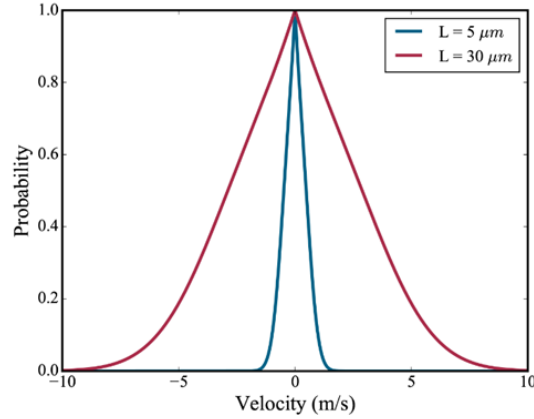


Fig. S3. Transverse velocity distribution for cell thickness of $5\mu\text{m}$ (blue) and $30\mu\text{m}$ (red).

5. Extraction of the nonlinear Faraday rotation effect

Here we present a simplified 2D model for the transverse velocity distribution, which closely describes our experimental geometry due to its radial symmetry. The longitudinal and transverse velocities of the particles are correlated based on their direction of movement (see Fig. 1 in the main text).

The measured Faraday rotation spectra were analyzed under two different experimental conditions, as illustrated in Fig. S4. When the pumping beam was turned off, only the linear Faraday effect was observed as the magnetic field was scanned. This condition serves as a baseline to assess the linear optical response of the system. In contrast, when the pumping beam was turned on, coherent atoms not affected by wall collisions propagated into the probing beam area within the cell, resulting in an additional nonlinear Faraday effect. By subtracting the 'Pump off' measurements from the 'Pump on' measurements, we obtained a clear representation of the pure nonlinear rotation component.

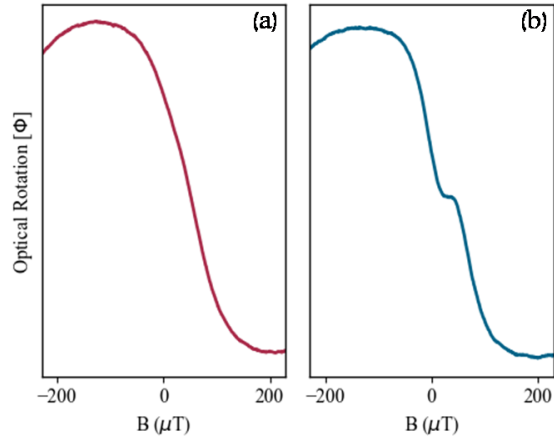


Fig. S4. Measured Faraday rotation spectra under different experimental conditions: (a) Pumping beam off – only the linear Faraday effect occurs as the magnetic field is scanned; (b) Pumping beam on —atoms not affected by wall collisions propagate coherently into the probing beam area, causing an additional nonlinear Faraday effect. The difference between the 'Pump off' and 'Pump on' measurements represents the pure nonlinear rotation component.

References

1. N. W. Ressler, R. H. Sands, and T. E. Stark, *Measurement of Spin-Exchange Cross Sections for Cs133, Rb87, Rb85, K39, and Na*, Physical Review **184**, 102 (1969).
2. D. Budker and M. Romalis, *Optical Magnetometry*, Nat Phys **3**, 227 (2007).